Structure
Article

Structural Underpinnings of Nitrogen Regulation by the Prototypical Nitrogen-Responsive Transcriptional Factor NrpR

Goragot Wisedchaisri,[1,7] David M. Dranow,[1,7] Thomas J. Lie,[2] Jeffrey B. Bonanno,[3] Yury Patskovsky,[3] Sinem A. Ozyurt,[4] J. Michael Sauder,[4] Steven C. Almo,[3] Stephen R. Wasserman,[5] Stephen K. Burley,[4] John A. Leigh,[2] and Tamir Gonen[1,6,*]
[1]Department of Biochemistry
[2]Department of Microbiology
University of Washington, Seattle, WA 98195, USA
[3]Department of Biochemistry, Albert Einstein College of Medicine, Bronx, NY 10461, USA
[4]Eli Lilly and Company, Lilly Biotechnology Center, San Diego, CA 92121, USA
[5]Eli Lilly and Company, LRL-CAT, Advanced Photon Source, Argonne National Laboratory, Argonne, IL 60439, USA
[6]Howard Hughes Medical Institute, University of Washington, Seattle, WA 98195, USA
[7]These authors contributed equally to this work
*Correspondence: tgonen@u.washington.edu
DOI 10.1016/j.str.2010.08.014

SUMMARY

Plants and microorganisms reduce environmental inorganic nitrogen to ammonium, which then enters various metabolic pathways solely via conversion of 2-oxoglutarate (2OG) to glutamate and glutamine. Cellular 2OG concentrations increase during nitrogen starvation. We recently identified a family of 2OG-sensing proteins—the nitrogen regulatory protein NrpR—that bind DNA and repress transcription of nitrogen assimilation genes. We used X-ray crystallography to determine the structure of NrpR regulatory domain. We identified the NrpR 2OG-binding cleft and show that residues predicted to interact directly with 2OG are conserved among diverse classes of 2OG-binding proteins. We show that high levels of 2OG inhibit NrpRs ability to bind DNA. Electron microscopy analyses document that NrpR adopts different quaternary structures in its inhibited 2OG-bound state compared with its active apo state. Our results indicate that upon 2OG release, NrpR repositions its DNA-binding domains correctly for optimal interaction with DNA thereby enabling gene repression.

INTRODUCTION

Nitrogen is an essential element for life as it is a central component in the building blocks for both nucleic acids and proteins. Environmental nitrogen typically exists in its oxidized form, but virtually all biological systems contain nitrogen in its reduced form. Both plants and microorganisms can acquire inorganic nitrogen directly (NO_3^- and N_2) and reduce it to ammonium (Stitt et al., 2002; Richardson et al., 2001; Cheng, 2008). Ammonium subsequently enters various metabolic pathways, through the conversion of 2-oxoglutarate (2OG, also known as α-ketoglutarate) to glutamate and glutamine (Leigh and Dodsworth, 2007). 2OG also plays a crucial role as one of the key metabolites in the TCA cycle and amino acid metabolism. Members of the animal kingdom, on the other hand, are not able to reduce environmental nitrogen into its usable form, and, therefore, acquire nitrogen exclusively from catabolism of dietary proteins and organic nitrogen compounds.

Nitrogen uptake is tightly regulated with 2OG playing a key role. 2OG reflects intracellular nitrogen levels as its concentration increases during nitrogen starvation (Leigh and Dodsworth, 2007). Several 2OG-sensing proteins bind 2OG and subsequently alter the activities of enzymes, transport proteins, or regulators in the nitrogen acquisition pathways (Leigh and Dodsworth, 2007). The most widespread 2OG-sensing proteins are from the P_{II} protein family found in eubacteria and some archaeal species (Leigh and Dodsworth, 2007). Members of the P_{II} family utilize 2OG and ATP to regulate nitrogen assimilation by modulating the activities of ammonium transporters, transcription regulators, and covalent modifying enzymes (Leigh and Dodsworth, 2007). A recent study of an archaeal P_{II} protein $GlnK_1$ shows that the binding of ATP and 2OG regulates the conformation of a protruding tyrosine-loop (T-loop), which is important for binding to the ammonium transporter Amt1 (Yildiz et al., 2007). A second family of 2OG-sensing proteins related to the P_{II} family is the NifI family (Dodsworth et al., 2005; Dodsworth and Leigh, 2006). $NifI_1$ and $NifI_2$ proteins form an active heterohexamer that regulates nitrogen fixation by inhibiting nitrogenase activities (Dodsworth et al., 2005). Binding of 2OG and ATP alters the oligomeric states of $NifI_1/I_2$ from a hexamer to the inactive dodecameric form (Dodsworth and Leigh, 2006). In addition to the P_{II} and NifI proteins, 2OG interacts directly with many other nitrogen regulatory or assimilatory proteins (Leigh and Dodsworth, 2007) making 2OG a ubiquitous indicator of nitrogen levels in cells.

Recently, a novel family of 2OG-sensing proteins was found primarily in the kingdom of Euryarchaeota and termed the nitrogen regulatory protein NrpR (Lie and Leigh, 2003; Lie et al., 2005). In contrast to other 2OG-sensing proteins, NrpR proteins do not require ATP for activity. Moreover, NrpR proteins are transcription factors that interact directly with DNA and function as repressors regulating transcription of nitrogen

assimilation genes. For example, NrpR recognizes and binds to a specific palindromic "nitrogen operator" sequence in the upstream promoter regions of the *glnA* gene and the $glnK_1$ and *nif* operons (Lie and Leigh, 2003). The *glnA* gene encodes a glutamine synthetase required for the conversion of glutamate to glutamine in the ammonium assimilation pathway. The *nif* operon gene cluster includes genes for nitrogen fixation (such as nitrogenases NifD and NifK) and 2OG-responsive P_{II} proteins $NifI_1$ and $NifI_2$ that regulate NifD and NifK. The $glnK_1$ operon encodes several P_{II} proteins ($GlnK_1$, $GlnK_2$, and GlnB) plus the ammonium transporters ($AmtB_1$ and $AmtB_2$) that are directly responsible for ammonium uptake. Cellular 2OG concentrations increase during nitrogen starvation. At increased concentrations, 2OG binds NrpR and inhibits DNA binding and transcriptional regulation resulting in expression of nitrogen assimilation genes. Together NrpR and 2OG, therefore, control expression of most proteins involved in nitrogen assimilation. Despite a wealth of genetic and biochemical data, the structural bases for 2OG-sensing and transcriptional regulation by NrpR remain unknown.

We have used a combination of X-ray crystallography and electron microscopy to study the structure of NrpR, both in its inhibited and active states. We report a 2.5 Å resolution structure of NrpR regulatory domain and together with in silico docking and mutagenesis studies identify the 2OG-binding cleft. We show that the 2OG-binding cleft is conserved among various NrpR proteins and that residues predicted to bind 2OG are conserved among diverse classes of 2OG-binding proteins. Electron microscopy was used to determine the structure of full-length NrpR both in its inhibited 2OG-bound state as well as its active apo state. Fitting of the crystal structure into the electron microscopy maps allowed us to model the two conformational states of the NrpR protein. Our data allow us to propose a mechanism for 2OG sensing by the transcriptional factor family of NrpR proteins and for allosteric regulation of DNA binding and transcriptional regulation of nitrogen assimilation.

RESULTS AND DISCUSSION

Crystal Structure of the NrpR Regulatory Domain

Like most other NrpR proteins, NrpR from the thermophilic archaeon *Methanocaldococcus jannaschii* (*Mj*NrpR) contains the putative N-terminal winged helix-turn-helix (wHTH) domain used for DNA binding followed by two NrpR regulatory domains (NRD1 and NRD2) that sense and bind 2OG (Lie and Leigh, 2007) (Figure 1A). The full-length protein resisted crystallization despite our very best efforts. Nevertheless, we were successful in crystallizing the second domain repeat of the NrpR regulatory domain (NRD2, residues 306–542) and determined its X-ray structure at 2.5 Å resolution (Figure 1B) using single-wavelength anomalous dispersion (SAD) phasing (Table 1). The asymmetric unit contained two NRD2 molecules (protomers A and B) related by noncrystallographic 2-fold symmetry (rmsd = 0.4 Å for common Cα atoms) (Figure 1C). Each protomer within the asymmetric unit is oval shaped and contains six α helices and ten β strands related to each other by an internal pseudo-2-fold symmetry, with each half of the protomer composed of three α helices and five β strands resembling the canonical ferredoxin fold (Bruschi and Guerlesquin, 1988) (Figure 1D; see Figure S1 available online). The first half of the protomer is composed of helices α4, α6, and α2 together with an antiparallel β sheet, made of strands β9-β1-β3-β2-β10. The second half of the protomer contains helices α1, α3, α5, and a β sheet, composed of strands β5-β4-β6-β8-β7 (Figure 1D). The apparent internal symmetry observed in the structure is not easy to detect at the sequence level, because the topology for NRD2 is highly intertwined between the two halves of the polypeptide chain (Figure S1). The helices from each half are located near the center of the NRD2 domain forming an α-helical layer onto which the β sheets are sandwiched from either side. A large cleft is formed between the two halves of the NRD2 regulatory domain (Figures 1D and 1E). This cleft contained an additional electron density feature that closely resembles glycerol, and probably originated from the crystallization buffer (Figure 1B).

2OG-Binding Site in NrpR

Surface analysis of NRD2 reveals a large cleft nearly 20 Å deep and 10 Å wide on one face of the molecule (Figure 1E). This cleft is formed by ~17 residues originating from helices α1, α3, and α-4, strands β1, β4, β6, β8, and β9, and loops connecting β3-α3, β5-α4, β8-α6 (Figures 1D and 2). Most of the residues forming the cleft are conserved among NrpR proteins from diverse organisms (Figure 2; Figure S2). An electron density feature corresponding to a bound glycerol molecule was observed deep in the center of the cleft forming hydrogen bonds with the side chains of Asn350, Tyr433, and Arg459, and the main chain nitrogen of Ala396, Gly508, and Ile509 (Figure 1F). The glycerol molecule also makes van der Waals contacts to the side chains of Cys395, Ala396, His441, and Ile509 (distances <4 Å). A water molecule bridges the glycerol molecule to Thr505 via hydrogen bonds. Electrostatic potential calculations reveal a large electrostatically positive surface feature where glycerol is bound, and a slightly electrostatically negative surface feature near the entry to the cleft (Figure 1E). Arg459 mainly contributes to the net positive potential within the cleft. All of the residues that form contacts with the glycerol molecule are highly conserved among NrpR proteins from diverse species, suggesting a functional role (Figure 2; Figure S2).

Mutational analysis of key residues from the glycerol-binding cleft, together with in silico simulations of 2OG-docking into our crystal structure, suggest that the glycerol-binding cleft is the site for 2OG-binding (Figure 3 and Table 2; Figure S3). We previously showed that amino acid residues involved in 2OG sensing and response are located in the NRD domains of NrpR (Lie and Leigh, 2007). Mutational analysis of NrpR from *Methanococcus maripaludis* (*Mm*NrpR) indicated that the two most critical residues for 2OG binding are Cys389 and His435 (Cys395 and His441, respectively, in *Mj*NrpR), while other mutations showed no significant effect (Table 2). Both the Cys395 and His441 are conserved among NrpR proteins from diverse species (Figure 2; Figure S2). In our crystal structure of the NRD2 domain, Cys395 and His441 are located deep within the cleft, where they make van der Waals contacts with glycerol.

Our docking results suggest that all of the glycerol-binding residues of NrpR are also involved in binding 2OG (Figures 1F and 3). We performed in silico docking simulations of 2OG onto our NRD2 crystal structure using AutoDock (Goodsell and Olson, 1990; Huey et al., 2007; Morris et al., 2009). We simulated 2OG docking into the NRD2 cleft by treating the NRD2 domain as

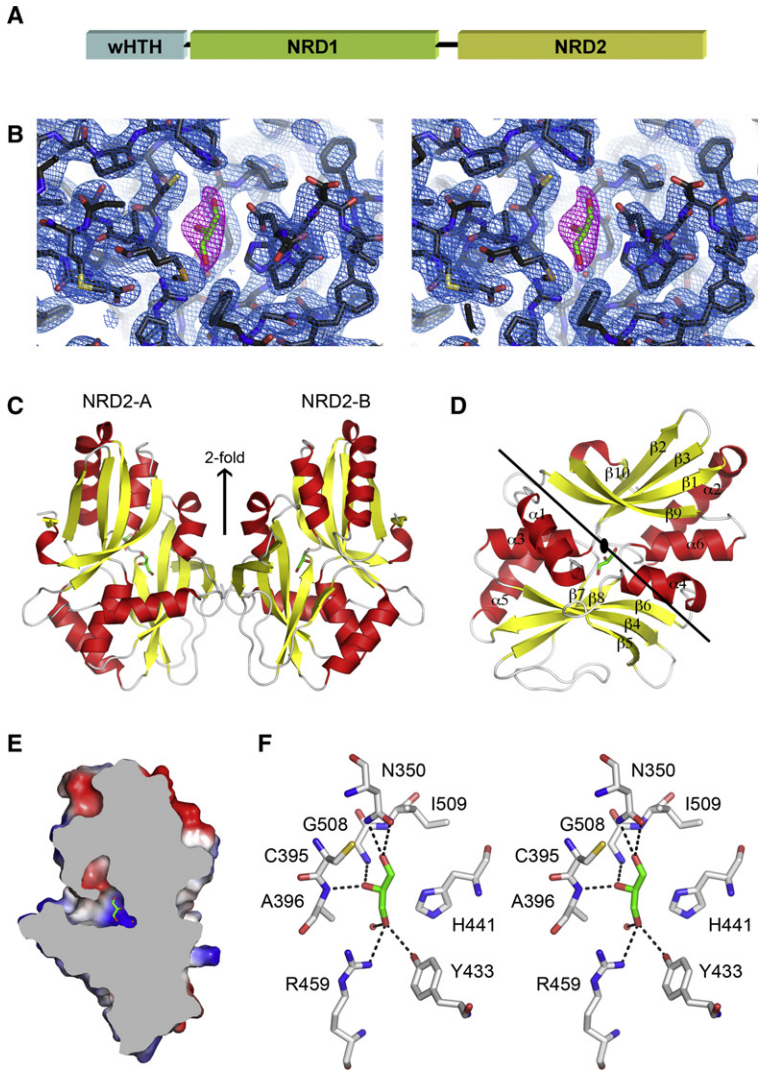

Figure 1. Crystal Structure of the NrpR Regulatory Domain 2 (NRD2)

(A) The domain architecture of NrpR. NrpR contains an N-terminal winged helix-turn-helix domain used for DNA binding, followed by two repeats of the NrpR regulatory domains (NRD1 and NRD2).

(B) Stereo view of the electron density map at 2.5 Å resolution near the 2OG-binding site. The σ_A-weighted $2F_o$-F_c electron density map for protein and water at 1σ level (blue) and the σ_A-weighted F_o-F_c omit map for glycerol at 2.75σ (magenta) are shown.

(C) Structure of the NRD2 domain. The asymmetric unit contains two NRD2 protomers related by a pseudo-2-fold rotational symmetry. Three glycerol molecules were also observed (green). Secondary structure elements are highlighted for α helices (red) and β strands (yellow).

(D) A close-up view of an NRD2 protomer. The domain can be grouped into two halves related by an internal 2-fold rotational symmetry (perpendicular to the plane). Each half contains three α helices and five β strands forming a β sheet. A cleft is formed in between the two halves of the NRD2 domain where a glycerol molecule was identified (green).

(E) Molecular surface display of the NRD2 domain. The surface is colored according to electrostatic potentials (blue = positive, red = negative). A positively charged cleft is located at the center of the domain internal symmetry where a glycerol molecule is bound. A water molecule is found at the deepest end of the cleft.

(F) Stereo view of the interactions between the glycerol molecule and amino acid residues forming the cleft. Several hydrogen bonds are formed between hydroxyl groups of glycerol and the side chain of Asn350, Tyr433, and Arg459, and the main chain amide of Ala396, Gly508, and Ile509. Side chains of Cys395, Ala396, and His441 contribute van der Waals interactions.

a rigid body and allowing 2OG to be flexible and to sample the entire space of the cleft. All docking results showed that 2OG converged to a single location deep within the cleft (Figure S3) (lowest calculated binding free energy of −4.1 kcal/mol corresponding to a K_d ~1 mM). This predicted value for K_d is comparable to the concentration of 2OG found in cells during nitrogen starvation and is sufficient to inhibit NrpR (Dodsworth et al., 2005; Lie et al., 2005). Our docking results suggest that 2OG prefers to adopt a *gauche* conformation at the C2-C3-C4-C5 dihedral angle, making the 2-carbonyl oxygen and the 5-carboxylate groups bend toward each other and form extensive contacts with residues in the NRD2 cleft (Figure 3A; Figure S3). 2OG is also predicted to form a salt bridge with Arg459 and several hydrogen bonds with side chains of Asn350, Tyr433, and His441, and the backbone amides of Ala396, Val397, Gly508, and Ile509 (Figure 3A). Finally, 2OG is predicted to make extensive van der Waals interactions with Met329, Cys395, Ala396, Val397, Asp439, His441, Met506, Gly507, and Ile509.

Structural Conservation among Diverse 2OG-Binding Proteins

The predicted 2OG-binding site in NrpR appears to be conserved among various 2OG-binding proteins from diverse species. NrpR utilizes similar amino acid side chain properties for binding to 2OG as observed in previously characterized 2OG-modifying enzymes, such as glutamate synthase, glutamate dehydrogenase, and anthocyanidin synthase (Figure 3). In contrast to the *gauche* conformation suggested by our docking calculations, 2OG binds to the active sites of these enzymes in the *anti* conformation at the C2-C3-C4-C5 dihedral angle. Residues Asn, Tyr/Ser, and Arg are commonly found in the 2OG-binding sites. Glutamate synthase, glutamate dehydrogenase, and anthocyanidin synthase all show hydrogen bonds analogous to that predicted between the C1 carboxylate group of 2OG and the side chain of Asn350 in NrpR. The C2 carbonyl group of 2OG in NrpR is predicted to form hydrogen bond to the backbone amide of Ala396, which resembles hydrogen bonds with 2OG seen in glutamate synthase and glutamate dehydrogenase. Another predicted hydrogen bond from the C2 carbonyl group of 2OG is directed to the backbone amide of Gly508 in NrpR, whereas C2 carbonyl oxygen of 2OG interacts with the side chain of a Lys residue in glutamate synthase and glutamate dehydrogenase. In addition, the C5 carboxylate group of 2OG is predicted to form a salt bridge and a hydrogen bond, respectively, to

Table 1. Data Collection and Refinement Statistics

Data collection	
Space group	$P3_121$
Unit-cell dimension (Å)	a = 80.01, b = 80.01, c = 116.42
Wavelength (Å)	0.9796
Resolution range[a] (Å)	50.0–2.5 (2.59–2.50)
Unique reflections	15,322
Completeness[a] (%)	99.2 (98.8)
Redundancy[a]	4.9 (3.8)
$I/\sigma(I)$[a]	7.1 (1.0)
R_{merge}[a]	0.075 (0.59)
TLS refinement	
Resolution range (Å)	40.0–2.50
Reflections used (working/free)	14,518/785
R_{work}	0.246
R_{free}	0.278
Average B-factor (Å^2)	55.6
Rmsds from ideal geometry	
Bonds lengths (Å)	0.008
Bond angles (deg.)	1.12
Ramachandran statistics	
Favored (%)	91.3
Allowed (%)	8.7
Disallowed (%)	0

[a] Values in parentheses are for the highest resolution shell.

Arg459 and Tyr433. Such interactions are similar to those observed in both glutamate synthase and anthocyanidin synthase. Many of the predicted van der Waals interactions between 2OG and NrpR are observed in glutamate dehydrogenase and anthocyanidin synthase.

A database search for similar protein structures as NRD2 using the Dali server (Holm et al., 2008) suggests that 2OG-responsive proteins share a common ancestry. Many of the proteins identified in the structure-based search contained the basic ferredoxin fold ($\beta_1\alpha_1\beta_2\beta_3\alpha_2\beta_4$) (Figure S1B) that is often present in nucleotide-binding or metal-binding proteins (Bruschi and Guerlesquin, 1988). (Interestingly, ferredoxin is also involved in the nitrogen assimilation pathway, mediating electron transfer for nitrogenases and glutamate synthase [Leigh, 2000]). A number of P_{II} proteins are among the top results of the structure-based search. Many of these P_{II}-proteins also share modest sequence identity (~14%–19%) with the NRD2 domain of NrpR (other hits that are non P_{II}-like proteins typically have sequence identities ~5%). Both NrpR and P_{II} proteins are involved in nitrogen regulation and 2OG sensing and binding (Leigh and Dodsworth, 2007). The highest score in our Dali structure-based search belonged to a putative P_{II}-like protein (PDB ID 3DFE) with a similar structure to our NRD2 (rmsd = 3.6 Å for 75 Cα atomic pairs; Figure S4). Although NrpR and P_{II} proteins are structurally and functionally similar, they differ in the way they bind 2OG in that NrpR neither contains a T-loop nor requires ATP for its function. Nevertheless, the structural similarity suggests that NrpR and P_{II} proteins evolved from a common ancestor.

NrpR Undergoes a Large Conformational Change upon 2OG Binding

Full-length *Mm*NrpR (60kDa) was purified and assayed using a DNA-gel shift assay for DNA-binding activity and inhibition by 2OG (Figure 4). Size-exclusion chromatography using a Superdex S200 column shows that NrpR eluted as a species corresponding in size to 120kDa indicating that NrpR forms a dimer (Figures 4A and 4B). Interestingly, our crystals contained two NRD2 molecules in the asymmetric unit (protomers A and B) (Figure 1C). The interface contacts are mediated by 18 residues making a total of 13 hydrogen bonds and three salt bridges creating a large buried surface of ~1700 Å^2 between NRD2 protomers A and B (Figure 1C; Figure S5). Fifteen of these 18 residues are highly conserved in NrpR (Figure 2, gray arrow heads) suggesting an important functional role and that the crystallographically observed AB dimer may represent how the two NRD2 domains interact within the full-length NrpR dimer.

We used a DNA-gel shift assay to test DNA binding by NrpR in the presence or absence of 2OG. A band shift was observed in the presence of NrpR, indicating formation of an NrpR-DNA complex (Figure 4C, lanes 1 and 4 versus 2 and 5). No significant band shift was observed upon addition of 2OG (Figure 4C, lanes 2 and 5 versus 3 and 6). The faint band shift observed in lanes 3 and 6 in Figure 4C suggests either that a minimal quantity of NrpR was not inhibited by 2OG or that 2OG dissociation during gel electrophoresis resulted in a subpopulation of NrpR able to bind DNA. Nevertheless, the vast majority of NrpR was inhibited by 2OG under the chosen experimental conditions.

To gain structural insights on the regulation of NrpR function by 2OG, we used electron microscopy and random conical tilt protocols (Radermacher et al., 1987) to determine 3D structures of full-length *Mm*NrpR both in its 2OG-bound (inhibited) and in its apo (active) forms (Figure 5). Initial characterization by electron microscopy of negatively stained preparations of NrpR indicated that the sample, although homogeneous by size-exclusion analysis (Figure 4), appears somewhat heterogeneous on the electron microscope grid (Figure 5A). While the particles appear uniform in size their quaternary structures are different. Some particles adopted a square-like shape and some adopted a "U" shape (Figure 5A, squares versus circles, respectively). These structural differences are best seen in projection averages (Figure 5A, right panels). We find that the presence or absence of 2OG markedly alters the distribution between these two particle types. In the NrpR + 2OG sample 62% are square shaped and 34% are U shaped while in the absence of 2OG only 12% are square shaped and the vast majority (81%) are U shaped (Figure 5A, inset table). We, therefore, performed three-dimensional reconstructions on the square shaped and U-shaped particles (Figures 5B and 5C, respectively). In the presence of 2OG, most NrpR molecules appeared as a square/trapezium-shaped particle with dimensions of 90 × 75 × 35 Å and a small hole in the center (Figure 5B). In the absence of 2OG, most NrpR molecules adopted a markedly different structure which resembles a "U" with dimensions of 80 × 90 × 35 Å (Figure 5C). Taken together, the data suggest that a major structural change occurs in NrpR in response to 2OG binding. It appears likely that there is equilibrium between the two conformational states of NrpR, and the absence or presence of 2OG shifts the equilibrium in one direction or the other.

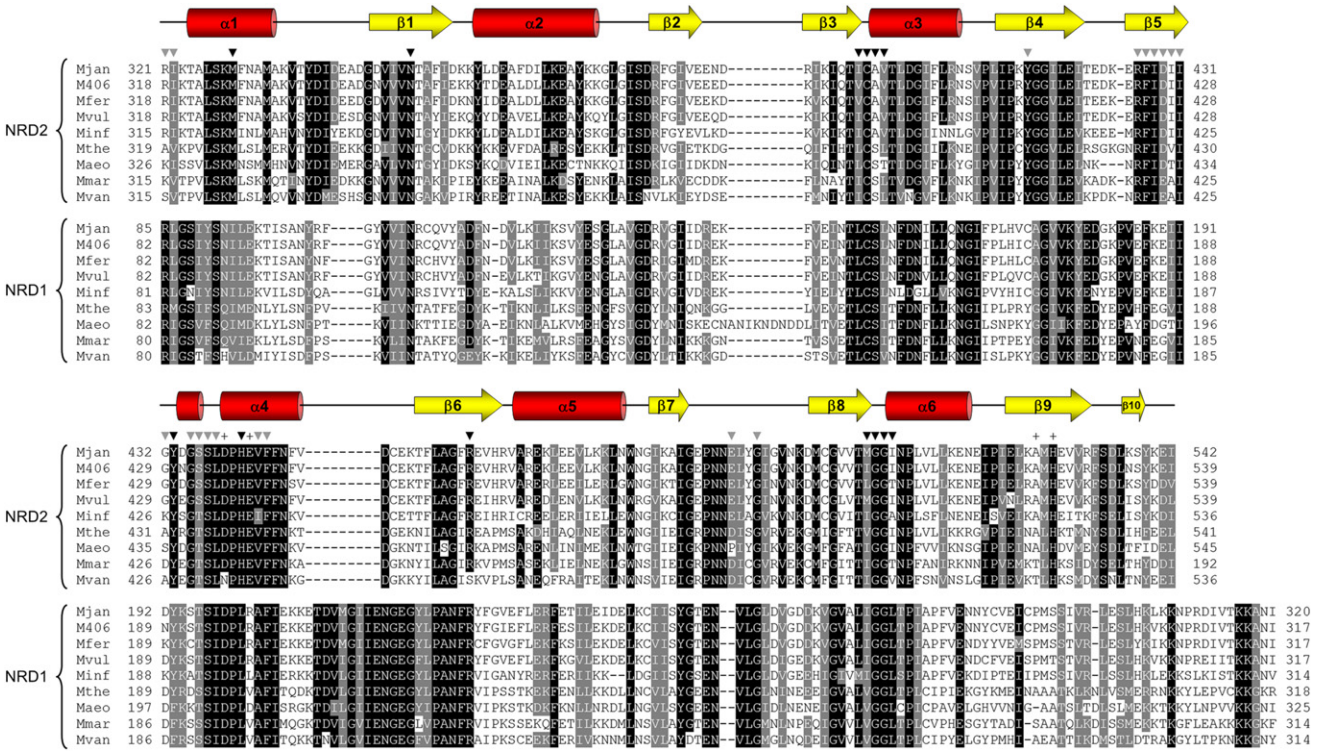

Figure 2. Sequence Alignment of the NrpR Regulatory Domains from *Methanocaldococcus* and *Methanococcus* Species

Residues with black and gray background shades are >90% identity and similarity, respectively. Secondary structure elements from the crystal structure of the *M. jannaschii* NRD2 domain are shown on top of the sequence alignment. Residues in the cleft that interact with glycerol and/or 2OG are indicated by black triangles while additional residues that form the cleft but do not interact directly with the ligands are indicated by +. Residues contributing to a dimerization interface are indicated by gray triangles. These residues appear to be functionally important and highly conserved in the sequence alignment. Mjan, *Methanocaldococcus jannaschii*; M406, *Methanocaldococcus sp*. FS406-22; Mfer, *Methanocaldococcus fervens*; Mvul, *Methanocaldococcus vulcanius*; Minf, *Methanocaldococcus infernus*; Mthe, *Methanococcus thermolithotrophicus*; Maeo, *Methanococcus aeolicus*; Mmar, *Methanococcus maripaludis*; *Mvan Methanococcus vannielii*.

In order to better understand this conformational change, we generated a pseudoatomic model of full-length NrpR by fitting our crystal structure of NRD2 and homology models of the wHTH domain and NRD1 (Figure 1A) into our experimental EM density maps. First, we used our crystal structure of NRD2 (Figure 1D) to generate a homology model of NRD1 using the ModWeb server (Eswar et al., 2003; Sanchez and Sali, 1998). NRD1 and NRD2 are both structurally and functionally homologous and share a high degree of sequence conservation (~50% identity). Next, for homology modeling the NrpR N-terminal wHTH domain, we used the structure of an iron-dependent regulator (IdeR) from *Mycobacterium tuberculosis* (Wisedchaisri et al., 2004, 2007). IdeR was chosen for as a template because its sequence alignment covers in its entirety the predicted wHTH domain of NrpR, and the crystal structure of the IdeR bound to DNA is available (Wisedchaisri et al., 2004). The first 56 residues in our model of the NrpR N-terminal wHTH domain form three α helices that are followed by a two-stranded β-hairpin (the wing) from residues 59–69. The most conserved region in the wHTH of NrpR is located on helix α3 where several Arg and Lys residues are located. These residues may participate in DNA binding and may be important for DNA base recognition, as seen for IdeR (Wisedchaisri et al., 2004).

The structures for all three domains of NrpR (wHTH, NRD1, and NRD2) were independently fit into the density maps of the 2OG-bound and apo-NrpR. Docking was performed in UCSF Chimera (Pettersen et al., 2004) and optimized until the models fit well within the two densities and no structural clashes were observed. As an internal positioning guide, we used gold conjugated Ni-NTA to localize the C-terminal His_6-tag on full-length NrpR (the NRD2 domain) (Figure 1A). The gold label localized to the bottom of the U-shaped apo-NrpR particle (data not shown). We, therefore, docked the NRD2 dimer from our crystal structure into the bottom of the NrpR "U"-shaped density feature. Importantly, this placement allowed us to maintain the observed dimeric arrangement of two NRD2 domains without major packing alterations. Next, we placed one NRD1 domain directly above each NRD2 domain. The remaining density at the very tip of the "U"-shaped particle was sufficient to accommodate the wHTH domains (Figure 5D). In the 2OG-bound state, NrpR appears as a square/trapezoid rather than a U-shaped particle (Figure 5). Conversion between the two structures can be achieved by a simple outward rotation of the wHTH domains coupled with an inward movement of the two NRD1 domains and a slight reorientation of NRD2 (Figure 5D).

Our pseudoatomic models suggest that NrpR exists in at least two conformations: a closed (2OG-bound) inhibited state and an open (apo-NrpR) active state. In the closed state, the two wHTH DNA-binding domains of NrpR are positioned ~80 Å from each other (Figure 5E, left). This interdomain distance is too far for

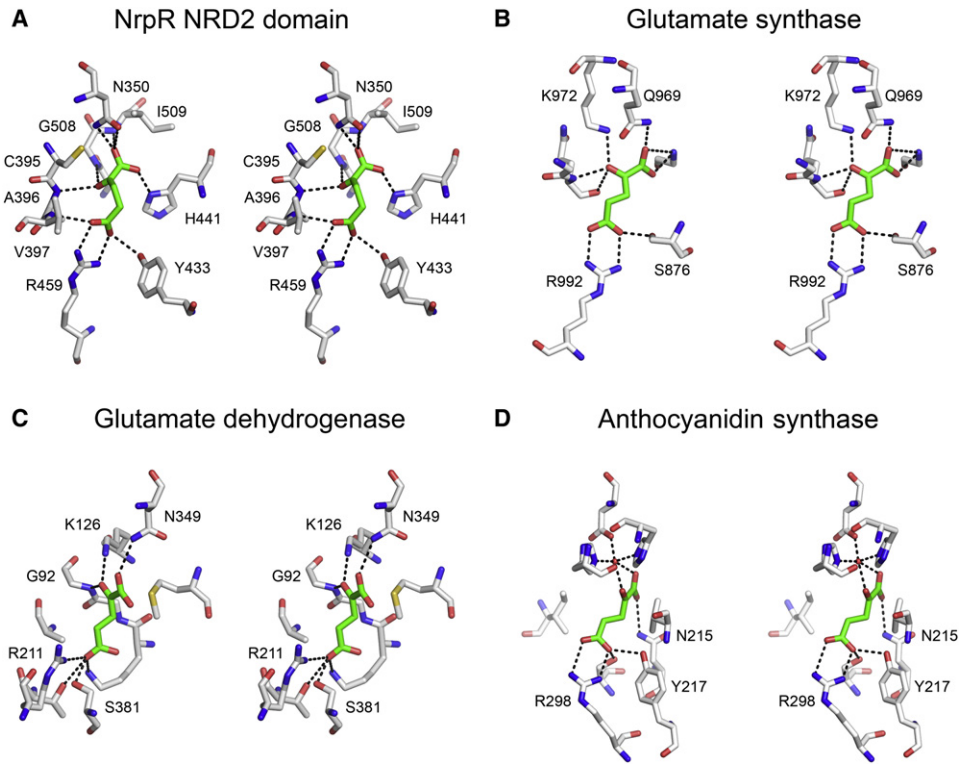

Figure 3. Structural Conservation of 2OG Binding in Various 2OG-Binding Proteins

(A) Stereo view of the 2OG binding interactions in the NRD2 domain from the docking experiments. The lowest energy conformation for 2OG binding is shown here. The ensemble of ten lowest energy conformations is supplemented in Figure S3. Residues making contacts with 2OG are highly conserved in the NRD domains. Similar binding environment for 2OG is observed in (B), Glutamate synthase (PDB 1OFD) (van den Heuvel et al., 2003), (C) Glutamate dehydrogenase (PDB 1HWY) (Smith et al., 2001), and (D) Anthocyanidin synthase (PDB 1GP4) (Wilmouth et al., 2002) and stereo views of the interactions are shown for all. Residues Asn, Tyr/Ser, and Arg form a conserved structural binding motif that make a hydrogen bond network to oxygen atoms of 2OG.

NrpR to be able to recognize the "nitrogen operator" DNA sequence, which is only ~45 Å in length. However, upon removal of 2OG, conformational rearrangement to the U-shaped conformation of NrpR brings the wHTH domains within ~45 Å of one another, thereby presenting them to the DNA operator (Figure 5E, right).

Table 2. Mutational Studies of 2OG Binding Residues

Species	Domain	Residues	Induction defect[a]
Methanococcus maripaludis	NRD1	C148A	+++
		S149A	–
		L195A	++
	NRD2	C389A	+++
		S390A	–
		H435A	+++
Methanopyrus kandleri	Single NRD	C167A	+++
		S168A	–
		S168P[b]	++
		S168F[c]	+++
		L214A	++

Analysis of previously published data from Lie and Leigh (2007).
[a] From no significant defect (–), to highly diminished (++), and abolished (+++) induction.
[b] Y36C/E93M/S168P/V297A mutant.
[c] R23Q/S168F/V182I mutant.

Concluding Remarks

Our study provides the first understanding at the molecular level on how nitrogen uptake is regulated by 2OG through the transcription regulator NrpR. It appears that the ferrodoxin fold in NrpR evolved to form a 2OG-binding cleft, which is conserved among various 2OG-modifying enzymes. During nitrogen starvation, cellular 2OG concentrations increase, thereby enabling binding to an inhibition of NrpR. Our EM findings suggest that in the 2OG-bound form, NrpR is inhibited from binding to DNA because its DNA-binding domains are too far apart to recognize the "nitrogen operator" DNA palindrome. As a result, transcription of nitrogen assimilation genes is turned on and intracellular nitrogen levels increase. Because nitrogen assimilation is energetically costly (16 ATP units per N_2 [Leigh, 2000]), this process must be tightly regulated. As cellular nitrogen levels rise, 2OG concentrations decrease and 2OG is released from NrpR. Following 2OG release, the NrpR dimer undergoes a conformational change to reconfigure the disposition of its DNA-binding domains, bind DNA, and repress expression of genes involved in nitrogen uptake. While our work has revealed the mechanism by which nitrogen assimilation is regulated in some detail, it is far from clear precisely how 2OG binding induces the

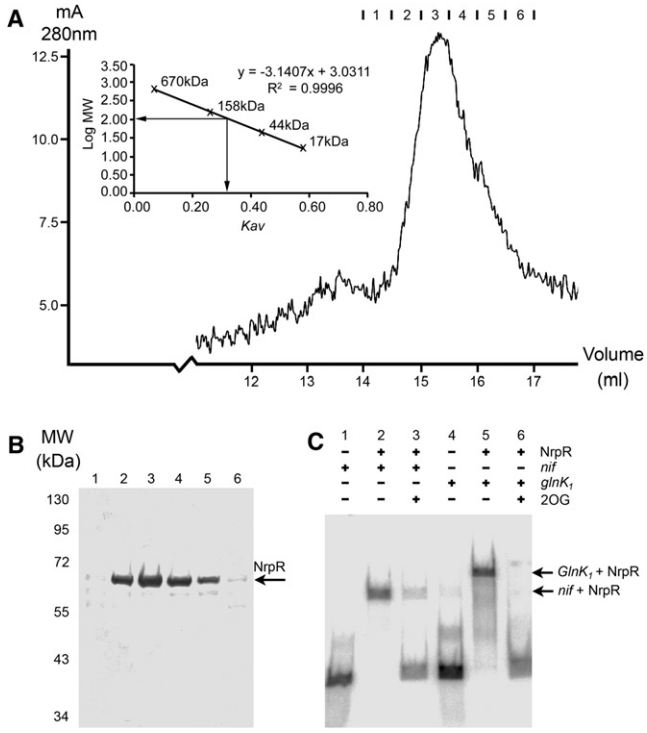

Figure 4. Purified Full-Length NrpR Is a Functional Dimer and Its DNA-Binding Function Can Be Modulated by 2OG

(A) Full-length His_6-tagged NrpR (60kDa) was purified using a combination of Ni^{2+}-NTA followed by size-exclusion chromatography on a Superdex 200 (S-200) column. The size-exclusion chromatogram is shown. NrpR eluted as a species corresponding to a molecular weight of 120 kDa indicating that NrpR is a dimer. Inset, calibration curve was constructed as described in the experimental procedure section.

(B) SDS-PAGE analysis of NrpR purification. Left, Molecular weight markers. The lanes correspond to the fractions indicated in (A) and the arrow points to NrpR.

(C) The DNA-binding function of NrpR was investigated using a DNA gel-shift assay (Lie and Leigh, 2003). DNA (0.03 nM) containing the sequence of the promoter region of either the *nif* (161 bp) (lanes 1–3) or $glnK_1$ (154 bp) (lanes 4–6) operon was incubated with purified NrpR (0.5 nM) (lanes 2 and 5). The binding of NrpR to the DNA causes the DNA to shift to a higher molecular weight in the gel (arrows). The presence of 10 mM 2OG in the protein-DNA mixtures (lanes 3 and 6) abolished the DNA-binding function of NrpR.

conformational change in NrpR at the atomic level and higher resolution studies are required. To date, crystallization efforts of full-length *Mm* and *Mj*NrpR have proven unsuccessful (whether 2OG was present or not) probably due to the structural equilibrium between the two NrpR states.

EXPERIMENTAL PROCEDURES

NRD2 Expression, Purification, and Crystallization

The gene for the NRD2 domain of *Mj*NrpR (residues 307–542) was amplified from genomic DNA by PCR, cloned into pSGX4 expression vector (N-terminal His_6-SUMO), and tested for expression and solubility in *Escherichia coli* BL21 (DE3) according to established methods (Sauder et al., 2008). SeMet protein was expressed in *E. coli* in High-Yield medium with SeMet buffer (Orion Enterprises, Inc, Northbrook, IL) at 22°C and purified using a nickel chelating column, followed by ULP1 protease cleavage of the SUMO (Smt3) fusion, a second nickel affinity column to remove the SUMO, and a Superdex 75 size exclusion column. Protocol details and results are provided in the Protein Expression Purification Crystallization Database (PepcDB, http://pepcdb.pdb.org) for targetID "NYSGXRC-10196a." The resulting protein starts with a Ser-Leu vector artifact (following SUMO cleavage) followed by residues 307–542 (UniProt Q57623); the Leu artifact matches wild-type L306, so the effective sequence is Ser-306-542. An average of 24 mg of purified SeMet protein was obtained per liter of culture. The purity and Se incorporation were assayed by SDS-PAGE analysis and mass spectrometry (ESI and MALDI), respectively. The molecular weight of the SeMet-labeled protein was 27,175 Da. The purified protein was concentrated to 9 mg/ml in buffer containing 10 mM HEPES (pH 7.5), 150 mM NaCl, 10% glycerol, and 1 mM β-mercaptoethanol or 5 mM dithiothreitol. Crystals were obtained in 100 mM sodium MES (pH 7.0) and 40% MPD, mixed with protein at 1 μl: 1 μl protein: precipitant ratio and equilibrated by vapor diffusion against 100 μl of precipitant at room temperature. Crystals were cryoprotected with 20% DMSO and flash frozen in liquid nitrogen prior to data collection.

Data Collection, Structure Determination, and Ligand Docking

Single wavelength anomalous diffraction data were collected at the selenium peak wavelength (λ = 0.9796 Å) at Argonne National Laboratory Advanced Photon Source Sector 31-ID and indexed in space group $P3_121$ to 2.5 Å resolution. Matthews' coefficient calculations indicated the presence of two molecules per asymmetric unit. Ten selenium sites were located using SHELXD and phases were calculated with SHELXE (Pape and Schneider, 2004). Several rounds of density modification together with automated and manual model building were performed in ARP/warp (Perrakis et al., 1999) and Coot (Emsley and Cowtan, 2004). Structure refinement was done in Refmac (Murshudov et al., 1997). Subsequently, cycles of density modification using Resolve (Terwilliger, 2002) were employed to improve phases followed by automated model building and refinement cycles. Best phases from Resolve were used for additional cycles of manual model building and refinement using Refmac (Murshudov et al., 1997). The refinement was completed with TLS restraint refinement. The structure contains two protomers of the NRD2 domain in the asymmetric unit (chain A: residues 321–540 and chain B: residues 319–539). Ligand docking of 2OG was performed in AutoDock4.1 using the AutoDockTools interface (Goodsell and Olson, 1990; Huey et al., 2007; Morris et al., 2009). The crystal structures of the NRD2 domain protomers A and B were used independently as docking receptors (as rigid bodies) while the 2OG molecule was allowed flexibility during the docking process. The Lamarckian genetic algorithm (Morris et al., 1998) was used to calculate an ensemble of ten models of 2OG docked into the crystal structure of the NRD2 domain (Figure S3).

Full-Length NrpR Purification and DNA-Binding Gel Shift Assay

Full-length His_6-tagged *Mm*NrpR was expressed in *M. maripaludis* strain Mm1048 using Ni^{2+}-NTA beads as described previously (Lie et al., 2005). Eluted NrpR was further purified by size-exclusion chromatography on a Superdex S200 column pre-equilibrated with 50 mM Tris-HCl (pH 7.5), 1 M NaCl, and 10% glycerol. For size measurements, the Superdex S200 column was calibrated using thyroglobulin (670 kDa), bovine γ-globulin (158 kDa), chicken ovalbumin (44 kDa), and myoglobin (17 kDa) standards (Bio-Rad), and blue dextran was used for determination of the void column volume. For the calculation of molecular size, a calibration plot of log MW versus K_{av} was constructed (Figure 4A, inset):

$$K_{av} = (V_e - V_0/V_t - V_0),$$

where V_e is the protein elution volume, V_t is the column volume and V_0 is the void column volume.

The DNA-binding gel shift assay was performed as described (Lie et al., 2005) with the exception that 7.2% (final concentration) of sucrose instead of glycerol was added to the binding mix just before loading of the samples into the gel. The *nif* and $glnK_1$ DNA probes were PCR amplified and labeled as described (Lie et al., 2010). Each DNA probe contains two palindromic "nitrogen operator" sites specific for NrpR binding but in a different configuration from the other. In the case of the *nif* promoter, the two nitrogen operators are located adjacent to each other in tandem separated by 30 base pairs on the same DNA strand. In the $glnK_1$ promoter, two nitrogen operators are overlapping from different DNA strands (Lie et al., 2010).

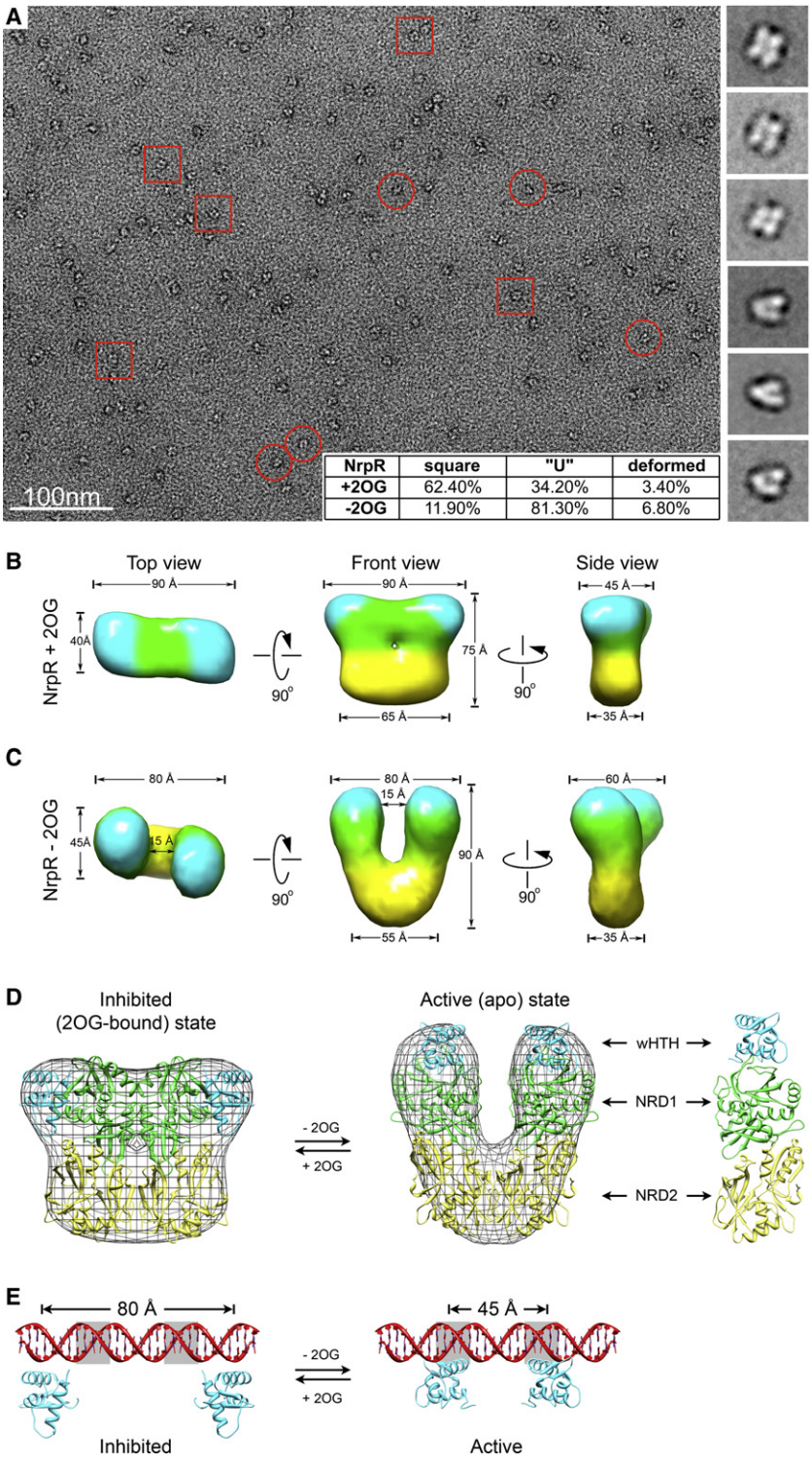

Figure 5. Electron Microscopy Analysis of Full-Length NrpR and the Molecular Mechanism for NrpR Inhibition by 2OG

(A) Electron microscopy of negatively stained NrpR indicates that while the particles are uniform in size their quaternary structures vary with two structures dominating the grid: square/trapezoid-like shape and "U" shape (red squares and circles, respectively). The two predominant conformations are better illustrated in the projection averages that are presented on the right panels. The presence or absence of 2OG modulates the distribution of NrpR conformations (table inset).

(B and C) 3D reconstruction for NrpR in complex with 2OG and apo-NrpR, respectively. In the presence of 2OG, NrpR adopts a compact, square/trapezoid-like shape while apo-NrpR displays a distinct U shape.

(D) Pseudoatomic model of full-length NrpR. The crystal structure of NRD2 domain (yellow) and homology models of NRD1 domain (green) and the wHTH domain (cyan) were fit into the NrpR density (mesh) both in the 2OG-bound (inactive) (left) and apo (active) (right) forms. The conformational change between the two forms appear to be the result of a simple outward rotation of the wHTH domains coupled with an inward movement of the two NRD1 domains.

(E) The positions of the DNA-binding domains of NrpR in the 2OG-bound and apo-state (left and right, respectively). In the inhibited state, the two wHTH DNA-binding domains of NrpR are positioned too far apart for NrpR to be able to bind the specific "nitrogen operator" DNA sequence (left). In the active form, the conformational change displaces the wHTH domains by ~35 Å closer together and brings them into the correct distance and orientation to allow them to bind DNA (right).

Electron Microscopy and Image Processing

Full-length *Mm*NrpR was expressed in *M. maripaludis* strain Mm500RC, purified using DNA affinity chromatography as described (Lie and Leigh, 2003) and stored at 4°C in 100 mM Tris HCl (pH 7.5), 1 M KCl, and 5 mM glycerol. A 2 μl drop of NrpR at a concentration of 10 μg/ml (with or without 10 mM 2OG) was applied to a carbon-coated grid, washed three times with milliQ water and stained using 0.075% uranyl formate as described (Zheng et al., 2010). The grid was mounted onto a Gatan high-tilt holder (±70°) and inserted into a FEI Tecnai Spirit equipped with a LaB_6 filament and operating at an accelerating voltage of 120 kV. Images of the negatively stained specimen were recorded on Kodak SO-163 film at a nominal magnification of 52,000× at the specimen level. Micrographs were digitized with a Nikon Super Cool Scan 9000ED and binned for a final pixel size of 4.2 Å. Particles for the 2OG-bound NrpR as well as apo NrpR were selected in WEB (8498 and 8200, respectively) and processed in SPIDER to produce initial 3D models using the random conical tilt method (Frank et al., 1996; Radermacher et al., 1987). These initial models were then used as reference models for angular refinement and reconstruction in SPIDER. The nominal resolution for the final reconstruction estimated from the spatial frequency at which the Fourier shell correlation fell to 0.5 (van Heel and Schatz, 2005) was ~22 and ~25 Å, respectively. Both density maps were filtered to 25 Å resolution and normalized in Mapman (Kleywegt and Jones, 1996) for comparison. The contour sigma threshold determined in SPIDER was 3.0 and 2.5σ above background, respectively. Density maps were visualized in UCSF Chimera (Pettersen et al., 2004) and figures were prepared using the above sigma levels.

Homology modeling and Structure Fitting into EM Maps

Homology models for the wHTH and of the NRD1 domains of NrpR were calculated using the ModWeb server (Eswar et al., 2003; Sanchez and Sali, 1998). A model of the wHTH domain of NrpR was generated based on the crystal structure of the iron-dependent regulator IdeR from *Mycobacterium tuberculosis* (PDB ID 1FX7) (Feese et al., 2001). Our structure of NRD2 was used for modeling the NRD1 domain of NrpR (residues 92–315) based on the high sequence (and functional) homology between the two domains. The wHTH, NRD1, and NRD2 were fit manually into the electron microscopy density map of full-length NrpR in UCSF Chimera (Pettersen et al., 2004). The positioning of the wHTH domains was guided by the crystal structure of IdeR-DNA complex (PDB ID 2ISZ) (Wisedchaisri et al., 2007). Gold-conjugated Ni-NTA (1:1000 dilution in 50 mM Tris-HCl [pH 7.5], 1 M NaCl, and 10% glycerol) was incubated with full-length His_6-tagged NrpR and analyzed by negative-stain electron microscopy to localize the NRD2 (C terminus of NrpR) in the particle (data not shown).

ACCESSION NUMBERS

The coordinates and structure factors have been deposited in the Protein Data Bank as entry 3NEK. Density maps of full-length NrpR (apo and inhibited) were deposited to the Electron Microscopy Database (EMD ID 5221 and 5222, respectively).

SUPPLEMENTAL INFORMATION

Supplemental Information includes five figures and can be found with this article online at doi:10.1016/j.str.2010.08.014.

ACKNOWLEDGMENTS

We thank the Murdock Charitable Trust and the Washington Research Foundation for generous support of our electron cryomicroscopy laboratory. We thank Brian Moore and Abigail Lambert for purification of NrpR protein. We also thank Yifan Cheng (University of California, San Francisco) and Christophe Verlinde (University of Washington) for helpful discussions. This work was funded in part by NIH grant GM-55255 to J.A.L. D.M.D. is supported in part by Public Health Service, National Research Service Award 2T32 GM007270 from the National Institute of General Medical Sciences. The NYSGXRC is supported by NIH Grant U54 GM074945 (Principal Investigator: S.K. Burley). Use of the Advanced Photon Source at Argonne National Laboratory was supported by the U. S. Department of Energy, Office of Science, Office of Basic Energy Sciences, under Contract No. DE-AC02-06CH11357. Use of the Lilly Research Laboratories Collaborative Access Team (LRL-CAT) beamline at Sector 31 of the Advanced Photon Source was provided by Eli Lilly & Company, which operates the facility. We gratefully acknowledge the contributions of all NYSGXRC personnel. T.G. is a Howard Hughes Medical Institute Early Career Scientist. The authors declare no competing financial interests.

Received: June 11, 2010
Revised: August 2, 2010
Accepted: August 13, 2010
Published: November 9, 2010

REFERENCES

Bruschi, M., and Guerlesquin, F. (1988). Structure, function and evolution of bacterial ferredoxins. FEMS Microbiol. Rev. *4*, 155–175.

Cheng, Q. (2008). Perspectives in biological nitrogen fixation research. J. Integr. Plant Biol. *50*, 786–798.

Dodsworth, J.A., and Leigh, J.A. (2006). Regulation of nitrogenase by 2-oxoglutarate-reversible, direct binding of a PII-like nitrogen sensor protein to dinitrogenase. Proc. Natl. Acad. Sci. USA *103*, 9779–9784.

Dodsworth, J.A., Cady, N.C., and Leigh, J.A. (2005). 2-Oxoglutarate and the PII homologues NifI1 and NifI2 regulate nitrogenase activity in cell extracts of Methanococcus maripaludis. Mol. Microbiol. *56*, 1527–1538.

Emsley, P., and Cowtan, K. (2004). Coot: model-building tools for molecular graphics. Acta Crystallogr. D Biol. Crystallogr. *60*, 2126–2132.

Eswar, N., John, B., Mirkovic, N., Fiser, A., Ilyin, V.A., Pieper, U., Stuart, A.C., Marti-Renom, M.A., Madhusudhan, M.S., Yerkovich, B., et al. (2003). Tools for comparative protein structure modeling and analysis. Nucleic Acids Res. *31*, 3375–3380.

Feese, M.D., Ingason, B.P., Goranson-Siekierke, J., Holmes, R.K., and Hol, W.G. (2001). Crystal structure of the iron-dependent regulator from Mycobacterium tuberculosis at 2.0-A resolution reveals the Src homology domain 3-like fold and metal binding function of the third domain. J. Biol. Chem. *276*, 5959–5966.

Frank, J., Radermacher, M., Penczek, P., Zhu, J., Li, Y., Ladjadj, M., and Leith, A. (1996). SPIDER and WEB: processing and visualization of images in 3D electron microscopy and related fields. J. Struct. Biol. *116*, 190–199.

Goodsell, D.S., and Olson, A.J. (1990). Automated docking of substrates to proteins by simulated annealing. Proteins *8*, 195–202.

Holm, L., Kaariainen, S., Rosenstrom, P., and Schenkel, A. (2008). Searching protein structure databases with DaliLite v.3. Bioinformatics *24*, 2780–2781.

Huey, R., Morris, G.M., Olson, A.J., and Goodsell, D.S. (2007). A semiempirical free energy force field with charge-based desolvation. J. Comput. Chem. *28*, 1145–1152.

Kleywegt, G.J., and Jones, T.A. (1996). xdlMAPMAN and xdlDATAMAN—programs for reformatting, analysis and manipulation of biomacromolecular electron-density maps and reflection data sets. Acta Crystallogr. D Biol. Crystallogr. *52*, 826–828.

Leigh, J.A. (2000). Nitrogen fixation in methanogens: the archaeal perspective. Curr. Issues Mol. Biol. *2*, 125–131.

Leigh, J.A., and Dodsworth, J.A. (2007). Nitrogen regulation in bacteria and archaea. Annu. Rev. Microbiol. *61*, 349–377.

Lie, T.J., and Leigh, J.A. (2003). A novel repressor of nif and glnA expression in the methanogenic archaeon Methanococcus maripaludis. Mol. Microbiol. *47*, 235–246.

Lie, T.J., and Leigh, J.A. (2007). Genetic screen for regulatory mutations in Methanococcus maripaludis and its use in identification of induction-deficient mutants of the euryarchaeal repressor NrpR. Appl. Environ. Microbiol. *73*, 6595–6600.

Lie, T.J., Wood, G.E., and Leigh, J.A. (2005). Regulation of nif expression in Methanococcus maripaludis: roles of the euryarchaeal repressor NrpR, 2-oxoglutarate, and two operators. J. Biol. Chem. *280*, 5236–5241.

Lie, T.J., Hendrickson, E.L., Niess, U.M., Moore, B.C., Haydock, A.K., and Leigh, J.A. (2010). Overlapping repressor binding sites regulate expression of the Methanococcus maripaludis glnK(1) operon. Mol. Microbiol. *75*, 755–762.

Morris, G.M., Goodsell, D.S., Halliday, R.S., Huey, R., Hart, W.E., Belew, R.K., and Olson, A.J. (1998). Automated docking using a Lamarckian genetic algorithm and an empirical binding free energy function. J. Comput. Chem. *19*, 1639–1662.

Morris, G.M., Huey, R., Lindstrom, W., Sanner, M.F., Belew, R.K., Goodsell, D.S., and Olson, A.J. (2009). AutoDock4 and AutoDockTools4: automated docking with selective receptor flexibility. J. Comput. Chem. *30*, 2785–2791.

Murshudov, G.N., Vagin, A.A., and Dodson, E.J. (1997). Refinement of macromolecular structures by the maximum-likelihood method. Acta Crystallogr. D Biol. Crystallogr. *53*, 240–255.

Pape, T., and Schneider, T.R. (2004). HKL2MAP: a graphical user interface for macromolecular phasing with SHELX programs. J. Appl. Crystallogr. *37*, 843–844.

Perrakis, A., Morris, R., and Lamzin, V.S. (1999). Automated protein model building combined with iterative structure refinement. Nat. Struct. Biol. *6*, 458–463.

Pettersen, E.F., Goddard, T.D., Huang, C.C., Couch, G.S., Greenblatt, D.M., Meng, E.C., and Ferrin, T.E. (2004). UCSF Chimera–a visualization system for exploratory research and analysis. J. Comput. Chem. *25*, 1605–1612.

Radermacher, M., Wagenknecht, T., Verschoor, A., and Frank, J. (1987). Three-dimensional reconstruction from a single-exposure, random conical

tilt series applied to the 50S ribosomal subunit of Escherichia coli. J. Microsc. *146*, 113–136.

Richardson, D.J., Berks, B.C., Russell, D.A., Spiro, S., and Taylor, C.J. (2001). Functional, biochemical and genetic diversity of prokaryotic nitrate reductases. Cell. Mol. Life Sci. *58*, 165–178.

Sanchez, R., and Sali, A. (1998). Large-scale protein structure modeling of the Saccharomyces cerevisiae genome. Proc. Natl. Acad. Sci. USA *95*, 13597–13602.

Sauder, M.J., Rutter, M.E., Bain, K., Rooney, I., Gheyi, T., Atwell, S., Thompson, D.A., Emtage, S., and Burley, S.K. (2008). High throughput protein production and crystallization at NYSGXRC. Methods Mol. Biol. *426*, 561–575.

Smith, T.J., Peterson, P.E., Schmidt, T., Fang, J., and Stanley, C.A. (2001). Structures of bovine glutamate dehydrogenase complexes elucidate the mechanism of purine regulation. J. Mol. Biol. *307*, 707–720.

Stitt, M., Muller, C., Matt, P., Gibon, Y., Carillo, P., Morcuende, R., Scheible, W.R., and Krapp, A. (2002). Steps towards an integrated view of nitrogen metabolism. J. Exp. Bot. *53*, 959–970.

Terwilliger, T.C. (2002). Automated structure solution, density modification and model building. Acta Crystallogr. D Biol. Crystallogr. *58*, 1937–1940.

van den Heuvel, R.H., Svergun, D.I., Petoukhov, M.V., Coda, A., Curti, B., Ravasio, S., Vanoni, M.A., and Mattevi, A. (2003). The active conformation of glutamate synthase and its binding to ferredoxin. J. Mol. Biol. *330*, 113–128.

van Heel, M., and Schatz, M. (2005). Fourier shell correlation threshold criteria. J. Struct. Biol. *151*, 250–262.

Wilmouth, R.C., Turnbull, J.J., Welford, R.W., Clifton, I.J., Prescott, A.G., and Schofield, C.J. (2002). Structure and mechanism of anthocyanidin synthase from Arabidopsis thaliana. Structure *10*, 93–103.

Wisedchaisri, G., Holmes, R.K., and Hol, W.G. (2004). Crystal structure of an IdeR-DNA complex reveals a conformational change in activated IdeR for base-specific interactions. J. Mol. Biol. *342*, 1155–1169.

Wisedchaisri, G., Chou, C.J., Wu, M., Roach, C., Rice, A.E., Holmes, R.K., Beeson, C., and Hol, W.G. (2007). Crystal structures, metal activation, and DNA-binding properties of two-domain IdeR from Mycobacterium tuberculosis. Biochemistry *46*, 436–447.

Yildiz, O., Kalthoff, C., Raunser, S., and Kuhlbrandt, W. (2007). Structure of GlnK1 with bound effectors indicates regulatory mechanism for ammonia uptake. EMBO J. *26*, 589–599.

Zheng, H., Taraska, J., Merz, A.J., and Gonen, T. (2010). The prototypical H+/galactose symporter GalP assembles into functional trimers. J. Mol. Biol. *396*, 593–601.